materials

MDPI

Article

The Effects of Niobium and Molybdenum on the Microstructures and Corrosion Properties of CrFeCoNiNbxMoy Alloys

Chun-Huei Tsau *, Yi-Hsuan Chen and Meng-Chi Tsai

Institute of Nanomaterials, Chinese Culture University, Taipei 111, Taiwan; psfohs1130@gmail.com (Y.-H.C.); asd99586@yahoo.com.tw (M.-C.T.)

* Correspondence: chtsau@staff.pccu.edu.tw

Abstract: The present work systematically investigated the effects of niobium and molybdenum on the microstructures and corrosion properties of high-entropy $CrFeCoNiNb_xMo_x$ and $CrFeCoNiNb_xMo_{1-x}$ alloys, the maximum content of (Nb + Mo) was 20 at.%. All of the alloys were prepared by arc melting under an argon atmosphere. In $CrFeCoNiNb_xMo_x$ alloys (x = 0.15, 0.3 and 0.5), increasing Nb and Mo content would change the microstructure of the alloy from a hypoeutectic structure ($x \leq 0.3$) to a hypereutectic one (x = 0.5). All of the $CrFeCoNiNbxMo_{1-x}$ alloys (x = 0.25, 0.5 and 0.75) had a hypereutectic microstructure. Only two phases were analyzed in these alloys, which were face-centered cubic (FCC) and hexagonal close packing (HCP). Increasing the content of Nb and Mo increases the hardness of the alloys by the effects of the solid solution strengthening and formation of the HCP phase. The potentiodynamic polarization curves of these alloys were also measured in 1 M sulfuric acid and 1 M sodium chloride solutions to evaluate the corrosion resistance of these alloys. The $CrFeCoNiNb_{0.3}Mo_{0.3}$ alloy had the smallest corrosion rate (0.0732 mm/yr) in 1 M deaerated H_2SO_4 solution, and the $CrFeCoNiNb_{0.15}Mo_{0.15}$ alloy had the smallest corrosion rate (0.0425 mm/yr) in 1 M deaerated NaCl solution. However, the $CrFeCoNiNb_{0.5}Mo_{0.5}$ alloy still had the best combination of corrosion resistance and hardness in the present study.

Keywords: high-entropy alloy; $CrFeCoNiNb_xMo_x$; $CrFeCoNiNb_xMo_{1-x}$; microstructure; hardness; corrosion

Citation: Tsau, C.-H.; Chen, Y.-H.; Tsai, M.-C. The Effects of Niobium and Molybdenum on the Microstructures and Corrosion Properties of CrFeCoNiNbxMoy Alloys. *Materials* **2022**, *15*, 2262. https://doi.org/10.3390/ma15062262

Academic Editor: Petrica Vizureanu

Received: 28 February 2022
Accepted: 17 March 2022
Published: 18 March 2022

1. Introduction

The alloys used in this study were prepared under the high-entropy alloy concept [1–3]. This high-entropy alloy concept provides researchers to develop new materials with suitable properties for applications. Researchers can smartly select the elements to prepare the materials, and many high-entropy alloys (HEAs) were thus produced with excellent mechanical, physical and chemical properties. Moreover, the shapes of high-entropy materials can be bulk alloys, thin films or coating alloys. For example, the casting, homogenization, cold rolling, recrystallization and deformation mechanism of equiatomic CoCrFeMnNi high-entropy alloy were well investigated [4,5]. The microstructures and compression properties of $CoCrFeNiTiAl_x$ high-entropy alloys were tested, and results indicated that the CoCrFeNiTiAl alloy had good compressive strength and elastic modulus [6]. The elements with a high melting point were selected to produce the refractory alloys, such as NbMoTaW, VNbMoTaW and HfTaTiNbZr-based alloys [7,8]. The high-entropy alloys can be prepared by mechanical alloying (MA) to obtain the alloys with nanocrystalline structures and enhance the properties [9,10].

Cobalt, chromium and nickel are wildly used to produce alloys with good corrosion resistance. Other elements are selected and added into CoCrNi alloy to change the microstructures and enhance the mechanical properties, such as CoCrFeMnNi alloy [11]. Co–CrFeNiSn has good passivation in sodium chloride solution compared with stainless

steels [12]. The $AlCoCrFeNiTi_{0.5}$ coating was fabricated by laser cladding coating and showed the optimal performance of corrosion and mechanical properties [13]. Minor additions of molybdenum could improve the corrosion resistance of the $AlCrFe_2Ni_2$ alloy by suppressing pit formation [14]. The addition of molybdenum could increase the corrosion resistance was observed in the $(CoCrFeNi)_{100-x}Mo_x$ high-entropy alloys [15]. The study on the $Al_{0.4}CrFe_{1.5}MnNi_{0.5}Mo_x$ alloys indicated that adding molybdenum can effectively improve the impedance of passive film and reduce the corrosion current density and thus form a more stable passivation film [16]. The non-equimolar $Cr_{19}Fe_{22}Co_{21}Ni_{25}Mo_{13}$ alloy possessed better corrosion resistance compared with 304 stainless steel in both deaerated 1 M HNO_3 and 1 M HCl solutions [17]. The corrosion resistance of FeCuNbSiB and $CrFeCoNiNb_x$ alloys can be improved by adding niobium [18,19].

In our previous study on the corrosion properties of FeCoNi and CrFeCoNi alloys [20], the FeCoNi alloy had a better corrosion resistance by comparing with CrFeCoNi alloy. After adding molybdenum, the corrosion resistance of FeCoNiMo was not as good as that of the CrFeCoNiMo alloy [21]. This indicates that chromium is a very important element in developing a corrosion-resistant alloy. Therefore, the present work studied the effect of adding Nb and Mo on the CrFeCoNi alloy and evaluated the potential of the application.

2. Materials and Methods

The $CrFeCoNiNb_xMo_x$ and $CrFeCoNiNb_xMo_{1-x}$ alloys were prepared by arc-melting under argon atmosphere after accurate weighting. Each melt was about 100 g. Table 1 lists the nominal compositions of the alloys. The microstructures of the alloys were examined by a scanning electron microscope (SEM, JEOL JSM-6335, JEOL Ltd., Tokyo, Japan) after regular metallurgical processes. The compositions of the alloys and the phases existing in the alloys were analyzed by an energy dispersive spectrometer (EDS). An X-ray diffractometer (XRD, Rigaku ME510-FM2, Rigaku Ltd., Tokyo, Japan) was used to identify the phases in the alloys, and the scanning rate was fixed at 0.04 degrees per second. A Vicker's hardness tester (Matsuzawa Seiki MV1, Matsuzawa Ltd., Akita, Japan) was used to measure the hardness of the alloys, and the loading force was 19.61 N (2000 gf).

Table 1. The nominal compositions of the as-cast alloys.

Alloys	Weight Percent					
	Cr	Fe	Co	Ni	Nb	Mo
$CrFeCoNiNb_{0.15}Mo_{0.15}$	20.49	22.00	23.22	23.13	5.49	5.67
$CrFeCoNiNb_{0.3}Mo_{0.3}$	18.43	19.79	20.89	20.81	9.88	10.20
$CrFeCoNiNb_{0.5}Mo_{0.5}$	16.25	17.46	18.42	18.35	14.52	14.99
$CrFeCoNiNb_{0.25}Mo_{0.75}$	16.22	17.42	18.38	18.31	7.24	22.44
$CrFeCoNiNb_{0.75}Mo_{0.25}$	16.29	17.50	18.46	18.40	21.83	7.52

The potentiodynamic polarization curves of the alloys were tested by a three-electrode electrochemical device (Autolab PGSTAT302N, Metrohm Autolab B.V., Utrecht, The Netherlands). One electrode was the specimens mounted in epoxy resin with an exposed area of 0.196 cm^2 (0.5 cm in diameter). The second electrode was a counter (a platinum wire). The third electrode was a reference one, which was a saturated silver chloride electrode (Ag/AgCl, SSE). This potential of the reference Ag/AgCl electrode was 0.197 V higher than the standard hydrogen electrode (SHE) at 25 °C [22]. All of the potentiodynamic polarization curves were tested at 30 °C, and the scanning rate of the potentiodynamic polarization test was 1 mV per second. Nitrogen bubbled through the process to degas the oxygen in the solutions. The solutions of 1 M sulfuric acid and 1 M sodium chloric solutions were prepared by reagent-grade acids and deionized water.

3. Results and Discussion

This work was divided into two parts to investigate the effect of Nb and Mo content on the effects of $CrFeCoNiNb_xMo_y$ alloys. Part 1 was the $CrFeCoNiNb_xMo_x$ alloys, and x was 0.15, 0.3 and 0.5. The same amount of Nb and Mo was added to the CrFeCoNi alloy. The microstructure revolution of $CrFeCoNiNb_xMo_x$ alloys were studied in this part; the relationships between the properties and the microstructures were also investigated. Part 2 studied the properties of $CrFeCoNiNb_xMo_{1-x}$ alloys, where x was 0.25, 0.5 and 0.75. This part studied the effect of different ratios of Nb and Mo on the microstructures and properties of the alloys. The total amount of Nb and Mo was fixed at one part (20 at.%) because the alloys would easily crack during solidification if an excess amount of Nb and Mo was added.

3.1. $CrFeCoNiNb_xMo_x$ Alloys

The microstructures of as-cast $CrFeCoNiNb_xMo_x$ alloys, x = 0.15, 0.3 and 0.5, are shown in Figure 1. In our previous study, the CrFeCoNi alloy had an FCC-structured granular microstructure and some Cr-rich precipitates with HCP structure [20]. After adding Nb and Mo, the microstructures of as-cast $CrFeCoNiNb_xMo_x$ alloys became dendritic ones. The dendrites of $CrFeCoNiNb_xMo_x$ alloys showed a single phase, and the interdendrities of $CrFeCoNiNb_xMo_x$ alloys showed a eutectic structure. Table 2 shows the chemical compositions of the alloys and the phases existing in the alloys. According to our previous study [23], the HCP phase had higher Nb and Mo content, and FCC had higher Cr- Fe and Ni content. Therefore, the FCC and HCP phases were easy to identify by detecting the compositions. The dendrites of $CrFeCoNiNb_{0.15}Mo_{0.15}$ and $CrFeCoNiNb_{0.3}Mo_{0.3}$ alloys were an FCC phase and the dendrites of $CrFeCoNiNb_{0.5}Mo_{0.5}$ alloy were an HCP-structured laves phase. All of the interdendrites of $CrFeCoNiNb_xMo_x$ alloys were a eutectic structure with two phases which were FCC and HCP phases (laves phase). This indicated that the alloy changed from a hypoeutectic alloy to a hypereutectic one. That is, $CrFeCoNiNb_{0.15}Mo_{0.15}$ and $CrFeCoNiNb_{0.3}Mo_{0.3}$ alloys were hypoeutectic alloys, and $CrFeCoNiNb_{0.5}Mo_{0.5}$ alloy was a hypereutectic alloy.

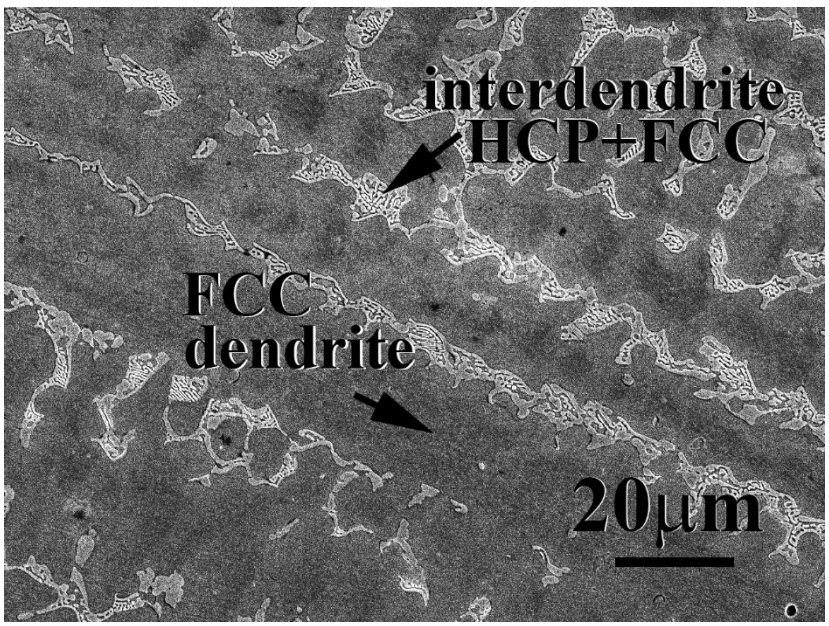

(**a**)

Figure 1. *Cont.*

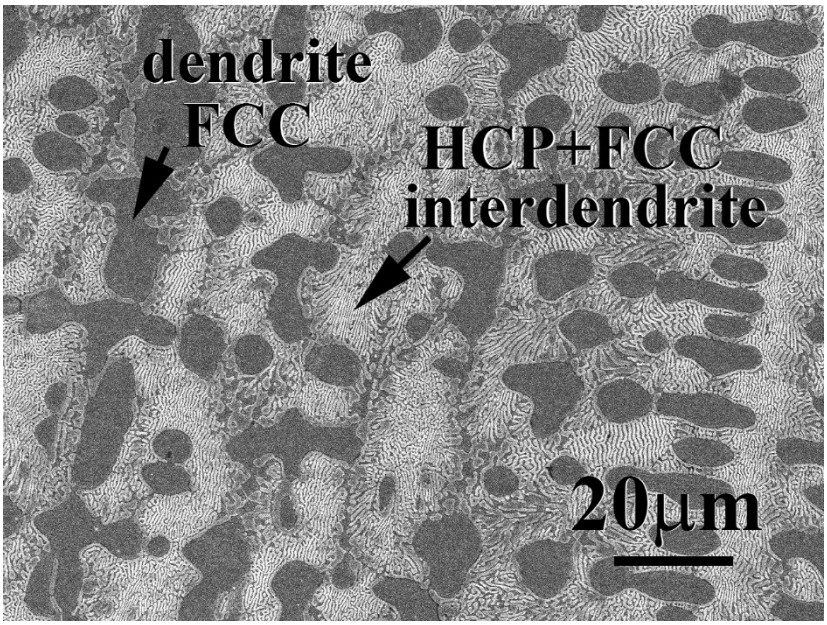

(**b**)

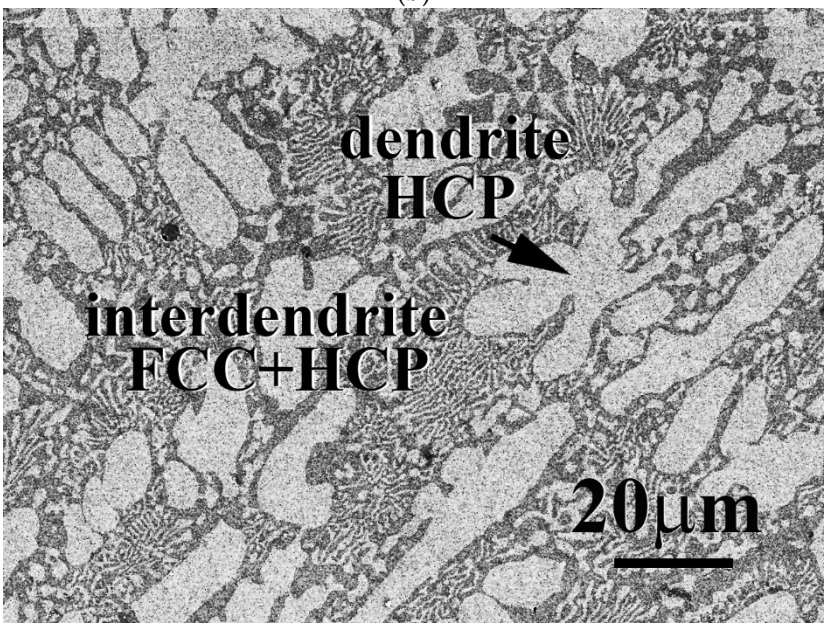

(**c**)

Figure 1. SEM micrographs of as-cast $CrFeCoNiNb_xMo_x$ alloys: (**a**) $CrFeCoNiNb_{0.15}Mo_{0.15}$ alloy; (**b**) $CrFeCoNiNb_{0.3}Mo_{0.3}$ alloy; (**c**) $CrFeCoNiNb_{0.5}Mo_{0.5}$ alloy.

Figure 2 shows the XRD patterns of the $CrFeCoNiNb_xMo_x$ alloys. Two phases of FCC and laves phases (HCP structure) were identified in these alloys. The FCC phase was the main phase in the $CrFeCoNiNb_{0.15}Mo_{0.15}$ alloy. Only a small amount of laves phase was in this alloy. Increasing the Nb and Mo content resulted in increasing the amount of laves phase. The laves phase became the major phase in the $CrFeCoNiNb_{0.5}Mo_{0.5}$ alloy. This result quite matches with the SEM observation.

Figure 3 plots the hardness of $CrFeCoNiNb_xMo_x$ alloys as a function of Nb and Mo content. Increasing Nb and Mo content would almost linearly increase the hardness of the $CrFeCoNiNb_xMo_x$ alloys. The hardness of $CrFeCoNiNb_{0.15}Mo_{0.15}$ alloy was only 215 HV, and the hardness of $CrFeCoNiNb_{0.5}Mo_{0.5}$ reached 553 HV. Adding Nb and Mo into CrFeCoNi alloy increases the hardness because the atomic radiuses of niobium and molybdenum are larger than those of the other elements. The atomic radiuses of niobium

and molybdenum are 1.43 and 1.40 Å, respectively; the atomic radiuses of cobalt, chromium, iron and nickel are 1.253, 1.249, 1.241 and 1.243 Å, respectively [24]. Therefore, the hardness of the $CrFeCoNiNb_xMo_x$ alloys increased due to the solid solution strengthening effect. Our previous work indicated that increasing niobium and molybdenum content increases the density of dislocation in the FCC phase [23]. This was another effect enhancing the hardness of the alloys. Additionally, the hardness of the HCP-structured laves phase was higher than that of the FCC phase because the slip system of the HCP phase was less than that of the FCC phase. The hardness of $CrFeCoNiNb_xMo_x$ alloys increased after adding more niobium and molybdenum elements due to the increase in the HCP phase and solid solution strengthening effect.

Table 2. The chemical compositions of the as-cast $CrFeCoNiNb_xMo_x$ alloys and the phases in each alloy analyzed by SEM/EDS.

Alloys	Weight Percent					
	Cr	Fe	Co	Ni	Nb	Mo
$CrFeCoNiNb_{0.15}Mo_{0.15}$						
overall	23.9 ± 0.9	24.2 ± 4.9	25.6 ± 0.4	17.2 ± 4.8	5.0 ± 0.2	4.1 ± 0.2
FCC	24.9 ± 1.3	25.3 ± 0.3	22.3 ± 1.1	20.5 ± 1.2	3.1 ± 0.7	3.9 ± 0.6
HCP	19.8 ± 0.5	16.0 ± 1.4	26.6 ± 1.3	16.6 ± 0.5	10.4 ± 0.3	10.6 ± 0.2
$CrFeCoNiNb_{0.3}Mo_{0.3}$						
overall	23.1 ± 1.3	20.4 ± 1.5	18.1 ± 2.1	21.7 ± 1.6	9.2 ± 0.5	7.5 ± 0.8
FCC	23.6 ± 2.0	23.3 ± 2.2	20.4 ± 2.8	25.8 ± 3.0	2.0 ± 0.4	5.1 ± 0.6
HCP	18.7 ± 0.6	14.6 ± 0.2	17.9 ± 2.6	17.8 ± 0.2	19.2 ± 0.2	11.8 ± 2.5
$CrFeCoNiNb_{0.5}Mo_{0.5}$						
overall	21.4 ± 0.4	19.4 ± 1.6	19.8 ± 0.3	17.6 ± 2.1	11.0 ± 0.2	10.8 ± 0.7
FCC	22.1 ± 0.9	20.4 ± 1.4	18.4 ± 0.3	22.8 ± 0.4	7.1 ± 1.2	9.2 ± 0.5
HCP	17.3 ± 0.3	23.6 ± 5.2	19.1 ± 0.8	14.2 ± 0.8	16.9 ± 0.1	15.6 ± 0.9

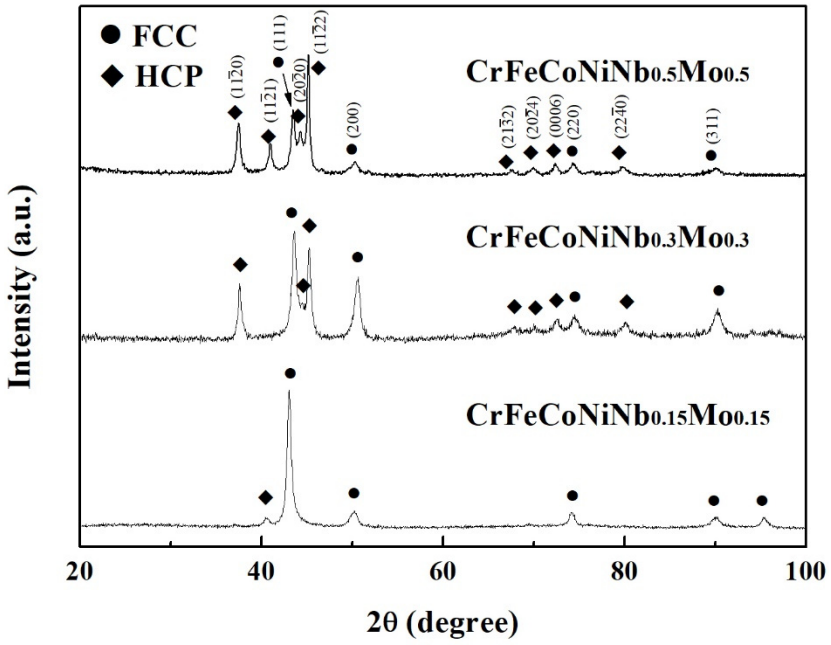

Figure 2. XRD patterns of as-cast $CrFeCoNiNb_xMo_x$ alloys.

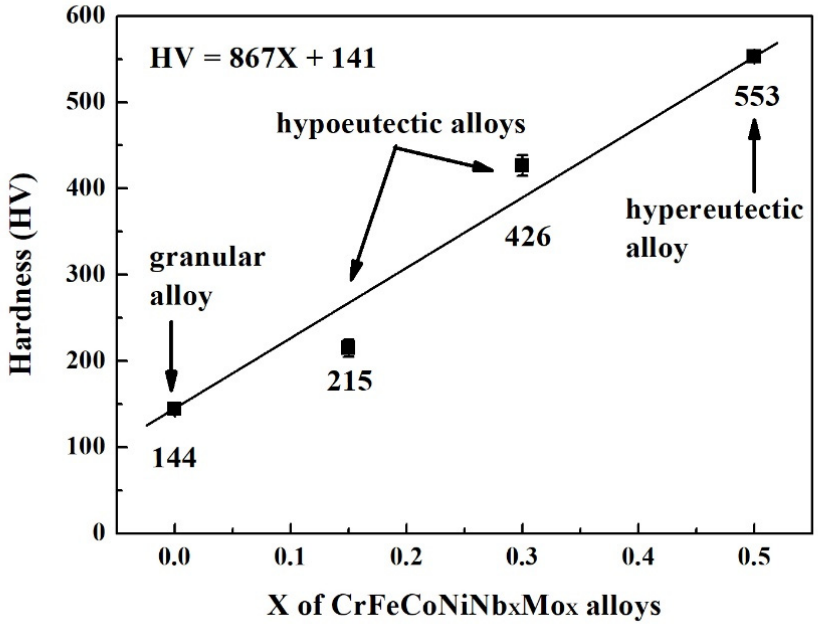

Figure 3. Hardness of as-cast $CrFeCoNiNb_xMo_x$ alloys. Each value is the average hardness of the alloy.

Figure 4 shows the potentiodynamic polarization curves of the as-cast $CrFeCoNiNb_xMo_x$ alloys in 1 M deaerated H_2SO_4 solution at 30 °C. The potentiodynamic polarization data of these polarization curves are listed in Table 3. The potentiodynamic polarization curves of the alloys with potential negative than corrosion potential (E_{corr}) was the cathode. The potentiodynamic polarization curves of the alloys with potential positive than corrosion potential was the anode. The corrosion potential (E_{corr}) of $CrFeCoNiNb_xMo_x$ alloys was very close. The standard electrode potential of the elements used in present work is listed in Table 4 [25]. The niobium is more active than the other elements because the standard electrode potential of niobium is more negative. Therefore, the corrosion potential of $CrFeCoNiNb_{0.5}Mo_{0.5}$ alloy had the most negative corrosion potential (E_{corr}). The corrosion current densities (i_{corr}) of $CrFeCoNiNb_xMo_x$ alloys were all around 10 $\mu A/cm^2$. The potentiodynamic polarization curve of $CrFeCoNiNb_{0.15}Mo_{0.15}$ alloy had an apparent anodic peak, and the other alloys had no anodic peak. The passivation potential (E_{pp}) and critical current density (i_{crit}) of the anodic peak of $CrFeCoNiNb_{0.15}Mo_{0.15}$ alloy is listed in Table 3. Thus, the $CrFeCoNiNb_{0.3}Mo_{0.3}$ and $CrFeCoNiNb_{0.5}Mo_{0.5}$ alloys easily entered into the passivation regions and formed the passive films during corrosion in H_2SO_4 solution. The lowest passivation current densities (i_{pass}) of these alloys were about 12 A/cm^2. All the passivation regions of these alloys were breakdown at a potential (E_b) of about 1.2 V (SHE) due to oxygen evolution reaction [26].

Table 3. Potentiodynamic polarization data of the as-cast $CrFeCoNiNb_xMo_x$ alloys in 1 M deaerated H_2SO_4 solution at 30 °C.

	$CrFeCoNiNb_{0.15}Mo_{0.15}$	$CrFeCoNiNb_{0.3}Mo_{0.3}$	$CrFeCoNiNb_{0.5}Mo_{0.5}$
E_{corr} (V vs. SHE)	−0.03	−0.05	−0.06
i_{corr} ($\mu A/cm^2$)	11.9	7.0	10.0
E_{pp} (V vs. SHE)	0.18	N/A	N/A
i_{crit} ($\mu A/cm^2$)	67.5	N/A	N/A
i_{pass} ($\mu A/cm^2$)	12.5	13.1	12.2
E_b (V vs. SHE)	1.21	1.19	1.19

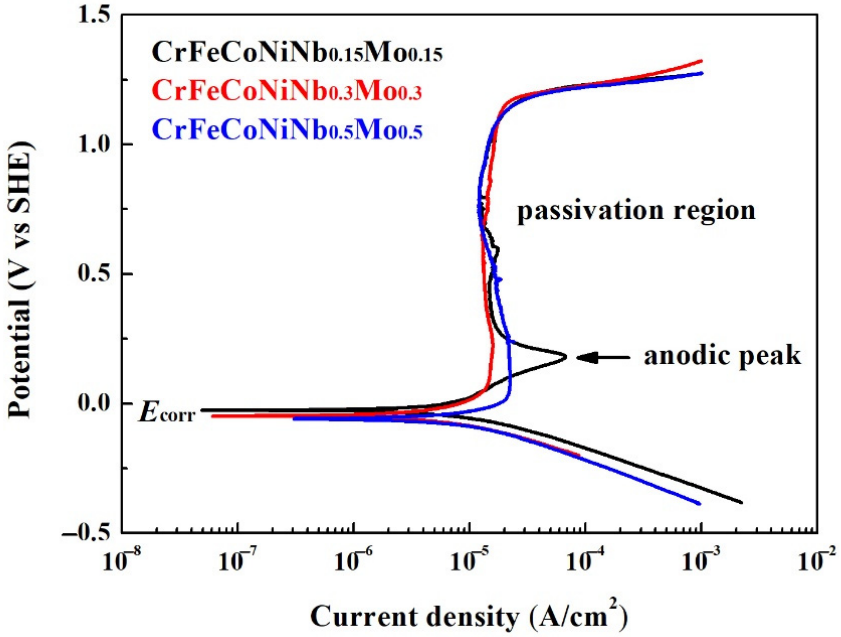

Figure 4. Potentiodynamic polarization curves of as-cast $CrFeCoNiNb_xMo_x$ alloys tested in the 1 M deaerated sulfuric acid solution at 30 °C.

Table 4. Standard electrode potential at 25 °C [25].

Reaction	Electrode Potential (E° vs. SSE)
Cr, Cr^{3+}	−0.74
Fe, Fe^{2+}	−0.44
Co, Co^{2+}	−0.227
Ni, Ni^{2+}	−0.25
Nb, Nb^{3+}	−1.10
Mo, Mo^{3+}	−0.20

Figure 5 displays the potentiodynamic polarization curves of the as-cast $CrFeCoNiNb_xMo_x$ alloys in 1 M deaerated NaCl solution at 30 °C. The potentiodynamic polarization data of these polarization curves are listed in Table 5. The corrosion potential (E_{corr}) of CrFeCoNi $Nb_{0.15}Mo_{0.15}$ alloy was more negative than the other alloys, and $CrFeCoNiNb_{0.15}Mo_{0.15}$ alloy also had the smallest corrosion current density (i_{corr}). All of the potentiodynamic polarization curves of $CrFeCoNiNb_xMo_x$ alloys in 1 M deaerated NaCl solution had apparent anodic peaks. Additionally, the potentiodynamic polarization curves of Cr–$FeCoNiNb_{0.15}Mo_{0.15}$ and $CrFeCoNiNb_{0.3}Mo_{0.3}$ alloys had small secondary anodic peaks. The $CrFeCoNiNb_{0.15}Mo_{0.15}$ alloy had the lowest passivation current density. The passivation current densities (i_{pass}) of these alloys were about 9–15 μA/cm^2.

3.2. $CrFeCoNiNb_xMo_{1-x}$ Alloys

The microstructures and properties of $CrFeCoNiNb_xMo_{1-x}$ alloys were studied in this part. The total amount of Nb and Mo of these alloys was kept as one part; the amount of Nb and Mo thus equaled 20 at.%. The microstructures of as-cast $CrFeCoNiNb_xMo_{1-x}$ alloys, x = 0.25 and 0.75, are shown in Figure 6. All of the $CrFeCoNiNb_xMo_{1-x}$ alloys, x = 0.25, 0.5 and 0.75, had a hypereutectic microstructure because a large amount of Nb and Mo were added into these alloys. The dendrites of $CrFeCoNiNb_xMo_{1-x}$ alloys were an HCP phase (laves phase), and the interdendrites of $CrFeCoNiNb_xMo_{1-x}$ alloys were a eutectic structure with FCC and HCP phases (laves phase). Table 6 lists the chemical compositions of the alloys and the phases existing in the alloys. As described above, the Nb and Mo content in the HCP phase of the alloys is higher than that in the FCC phase.

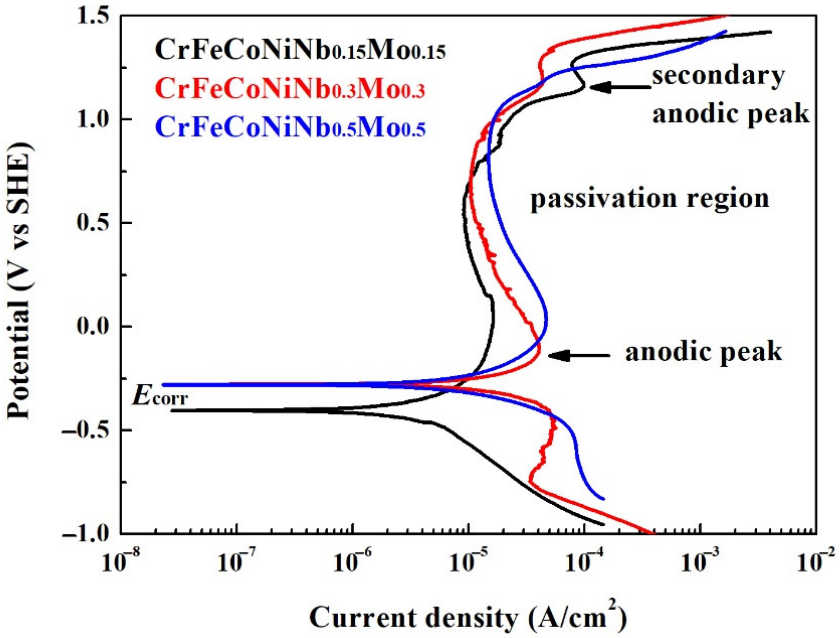

Figure 5. Potentiodynamic polarization curves of as-cast $CrFeCoNiNb_xMo_x$ alloys tested in the 1 M deaerated sodium chloric solution at 30 °C.

Table 5. Potentiodynamic polarization data of the as-cast $CrFeCoNiNb_xMo_x$ alloys in 1 M deaerated NaCl solution at 30 °C.

	$CrFeCoNiNb_{0.15}Mo_{0.15}$	$CrFeCoNiNb_{0.3}Mo_{0.3}$	$CrFeCoNiNb_{0.5}Mo_{0.5}$
E_{corr} (V vs. SHE)	−0.40	−0.28	−0.28
i_{corr} (μA/cm^2)	4.2	10.0	10.7
E_{pp} (V vs. SHE)	0.13	−0.10	0.03
i_{crit} (μA/cm^2)	16.2	40.9	47.0
i_{pass} (μA/cm^2)	9.1	10.5	15.0
E_b (V vs. SHE)	1.31	1.33	1.19

Table 6. The chemical compositions of the as-cast $CrFeCoNiNb_xMo_{1-x}$ alloys and the phases in each alloy analyzed by SEM/EDS.

Alloys	Weight Percent					
	Cr	Fe	Co	Ni	Nb	Mo
$CrFeCoNiNb_{0.25}Mo_{0.75}$						
overall	16.3 ± 3.4	17.6 ± 1.6	18.5 ± 1.0	18.1 ± 1.6	7.8 ± 1.3	21.7 ± 2.5
FCC	21.7 ± 2.2	21.2 ± 0.5	18.1 ± 1.9	25.6 ± 2.4	4.4 ± 3.3	9.0 ± 0.1
HCP	14.8 ± 2.3	15.2 ± 2.8	20.2 ± 1.5	15.4 ± 1.3	8.7 ± 0.2	25.7 ± 0.6
$CrFeCoNiNb_{0.75}Mo_{0.25}$						
overall	16.9 ± 0.6	17.5 ± 2.6	18.8 ± 2.0	18.9 ± 1.2	20.2 ± 0.2	7.7 ± 0.2
FCC	23.2 ± 2.5	23.8 ± 1.0	19.3 ± 0.6	27.7 ± 2.7	3.6 ± 0.1	2.4 ± 1.7
HCP	14.4 ± 0.6	15.5 ± 1.4	21.0 ± 0.4	14.1 ± 0.7	26.5 ± 1.1	8.5 ± 0.5

Figure 7 shows the XRD patterns of the $CrFeCoNiNb_xMo_{1-x}$ alloys. Two phases existing in these alloys were FCC and HCP-structured laves phases. The HCP phase was the main phase in these $CrFeCoNiNb_xMo_{1-x}$ alloys, and the FCC phase became the minor phase in these alloys. Figure 8 displays the hardness of $CrFeCoNiNb_xMo_{1-x}$ alloys, some of the data were from our previous study [23]. According to our previous study, the overall hardness of the alloy was contributed by the hard HCP dendrites and the soft interdendrities (HCP + HCC). The hardness of both HCP and FCC phases increased with increasing the content of Nb and Mo due to solid solution strengthening. However, the hardness of

the FCC phase was still softer than that of the HCP phase. Because the hardness of interdendrities was softer than that of dendrites, increasing the volume fraction of interdendrite would decrease the overall hardness of the alloy. The $CrFeCoNiNb_{0.5}Mo_{0.5}$ alloy had the lowest hardness among these alloys because of the largest ratio of interdendrities in this alloy. The $CrFeCoNiNb_{0.75}Mo_{0.25}$ alloy had the highest hardness of 625 HV among the alloys in the present study.

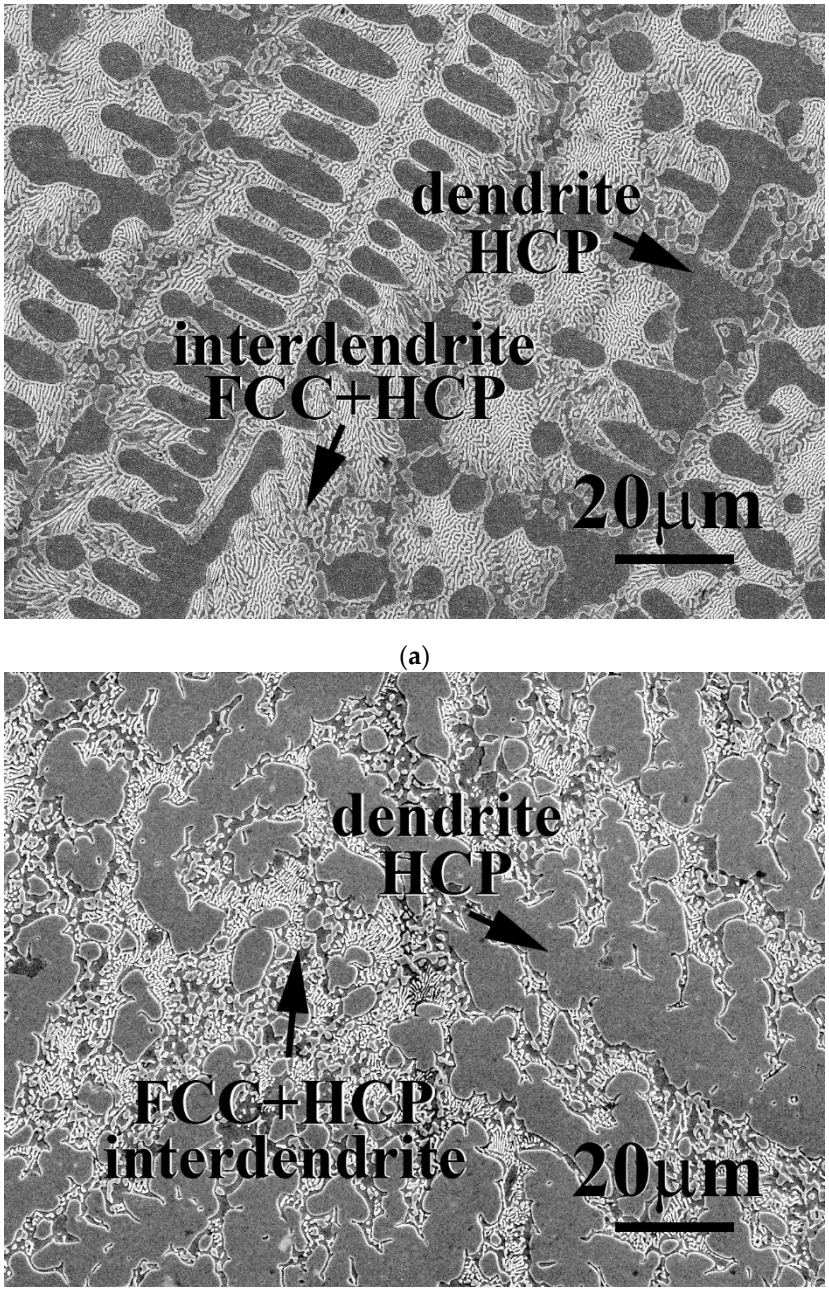

Figure 6. SEM micrographs of as-cast $CrFeCoNiNb_xMo_{1-x}$ alloys: (**a**) $CrFeCoNiNb_{0.25}Mo_{0.75}$ alloy and (**b**) $CrFeCoNiNb_{0.75}Mo_{0.25}$ alloy.

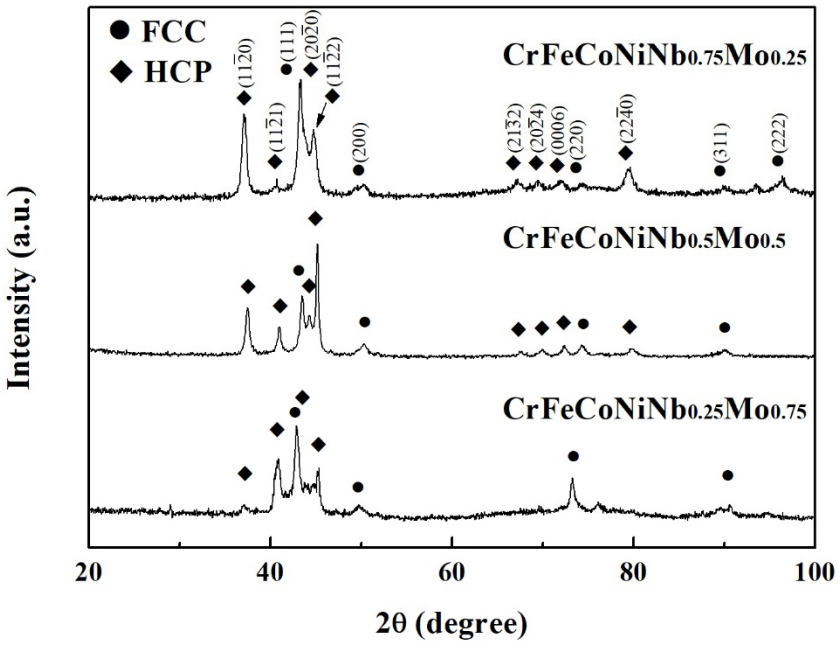

Figure 7. XRD patterns of as-cast $CrFeCoNiNb_xMo_{1-x}$ alloys.

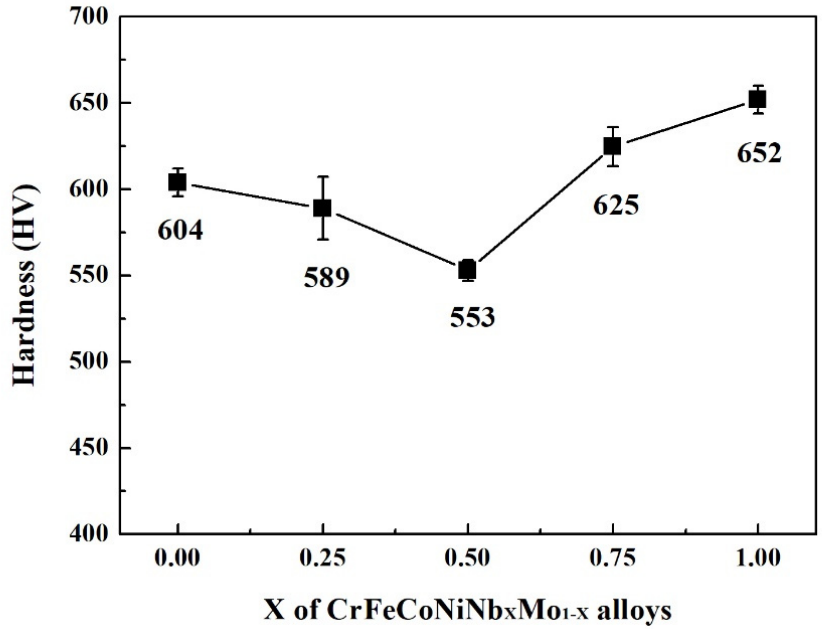

Figure 8. Hardness of as-cast $CrFeCoNiNb_xMo_{1-x}$ alloys. Each value is the average hardness of the alloy. Some of the data are from our previous study [23].

Figure 9 shows the potentiodynamic polarization curves of the as-cast $CrFeCoNiNb_xMo_{1-x}$ alloys in 1 M deaerated H_2SO_4 solution at 30 °C. The potentiodynamic polarization data of these polarization curves are listed in Table 7. The corrosion potential (E_{corr}) and the corrosion current densities (i_{corr}) of $CrFeCoNiNb_xMo_{1-x}$ alloys were very close; the $CrFeCoNiNb_{0.25}Mo_{0.75}$ alloy had the lowest i_{corr} of about 5 μA/cm^2. The potentiodynamic polarization curve of $CrFeCoNiNb_{0.25}Mo_{0.75}$ and $CrFeCoNiNb_{0.75}Mo_{0.25}$ alloys had apparent anodic peaks, but the $CrFeCoNiNb_{0.5}Mo_{0.5}$ alloy had no anodic peak. The passivation potential (E_{pp}) and critical current density (i_{crit}) of the anodic peaks of the alloys are listed in Table 7. This indicated that the $CrFeCoNiNb_{0.5}Mo_{0.5}$ alloys easily entered the passivation regions and formed the passive films during corrosion in H_2SO_4 solution among these alloys. The current densities of the passivation regions (i_{pass}) of $CrFeCoNiNb_{0.5}Mo_{0.5}$

and $CrFeCoNiNb_{0.75}Mo_{0.25}$ alloys were about 12 A/cm^2, but the $CrFeCoNiNb_{0.25}Mo_{0.75}$ alloy had a larger passivation current density (i_{pass}). The passivation regions of these alloys were all breakdown at a potential (E_b) of about 1.2 V (SHE) because of oxygen evolution reaction [26]. In order to compare the properties of corrosion potential, corrosion current density, anodic peak and passivation region of each alloy in the present study, the $CrFeCoNiNb_{0.5}Mo_{0.5}$ alloy had the best corrosion resistance among the alloys in H_2SO_4 solution.

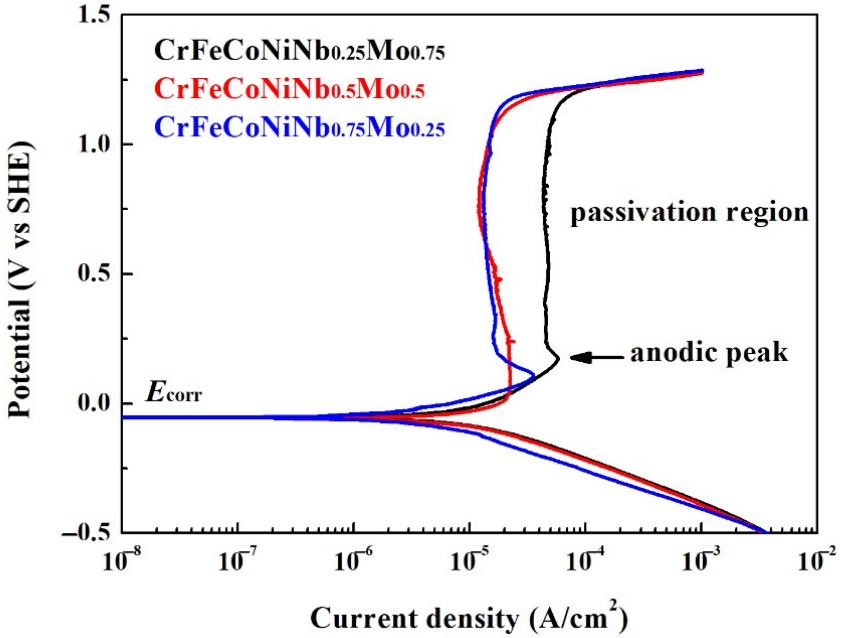

Figure 9. Potentiodynamic polarization curves of as-cast $CrFeCoNiNb_xMo_{1-x}$ alloys tested in the 1 M deaerated sulfuric acid solution at 30 °C.

Table 7. Potentiodynamic polarization data of the as-cast $CrFeCoNiNb_xMo_{1-x}$ alloys in 1 M deaerated H_2SO_4 solution at 30 °C.

	$CrFeCoNiNb_{0.25}Mo_{0.75}$	$CrFeCoNiNb_{0.5}Mo_{0.5}$	$CrFeCoNiNb_{0.75}Mo_{0.25}$
E_{corr} (V vs. SHE)	−0.06	−0.06	−0.06
i_{corr} (μA/cm^2)	10.2	10.0	4.9
E_{pp} (V vs. SHE)	0.17	N/A	0.11
i_{crit} (μA/cm^2)	58.3	N/A	35.7
i_{pass} (μA/cm^2)	44.1	12.2	11.9
E_b (V vs. SHE)	1.21	1.19	1.19

Figure 10 shows the potentiodynamic polarization curves of the as-cast $CrFeCoNiNb_xMo_{1-x}$ alloys in 1 M deaerated NaCl solution at 30 °C. The potentiodynamic polarization data of these polarization curves are listed in Table 8. The cathodic limit current density (i_L) was found in these $CrFeCoNiNb_xMo_{1-x}$ alloys. The cathodic limit current density meant that the maximum reaction rate was limited because of the diffusion rate of hydroxyl ions (OH^-) in the solution [26]. The corrosion potential (E_{corr}) of $CrFeCoNiNb_{0.25}Mo_{0.75}$ alloy was more positive than the other alloys; the corrosion potential (E_{corr}) of $CrFeCoNiNb_{0.5}Mo_{0.5}$ and $CrFeCoNiNb_{0.75}Mo_{0.25}$ alloy was very close. Moreover, the corrosion current density (i_{corr}) of $CrFeCoNiNb_{0.25}Mo_{0.75}$ alloy was larger than the other alloys. The corrosion current density (i_{corr}) of $CrFeCoNiNb_{0.5}Mo_{0.5}$ and $CrFeCoNiNb_{0.75}Mo_{0.25}$ alloys were about 10 μA/cm^2. All of the $CrFeCoNiNb_xMo_{1-x}$ alloys had apparent anodic peaks in 1 M deaerated NaCl solution. The passivation regions of $CrFeCoNiNb_{0.5}Mo_{0.5}$ and $CrFeCoNiNb_{0.75}Mo_{0.25}$ alloys were better than that of $CrFeCoNiNb_{0.25}Mo_{0.75}$ alloy. The minimum passivation current densities (i_{pass}) of $CrFeCoNiNb_{0.5}Mo_{0.5}$ and $CrFeCoNiNb_{0.75}Mo_{0.25}$

alloys were about 15 μA/cm^2. When comparing the properties of corrosion potential, corrosion current density, anodic peak and passivation region of each alloy in the present study, the CrFeCoNiNb$_{0.5}$Mo$_{0.5}$ alloy had the best corrosion resistance among the alloys in NaCl solution.

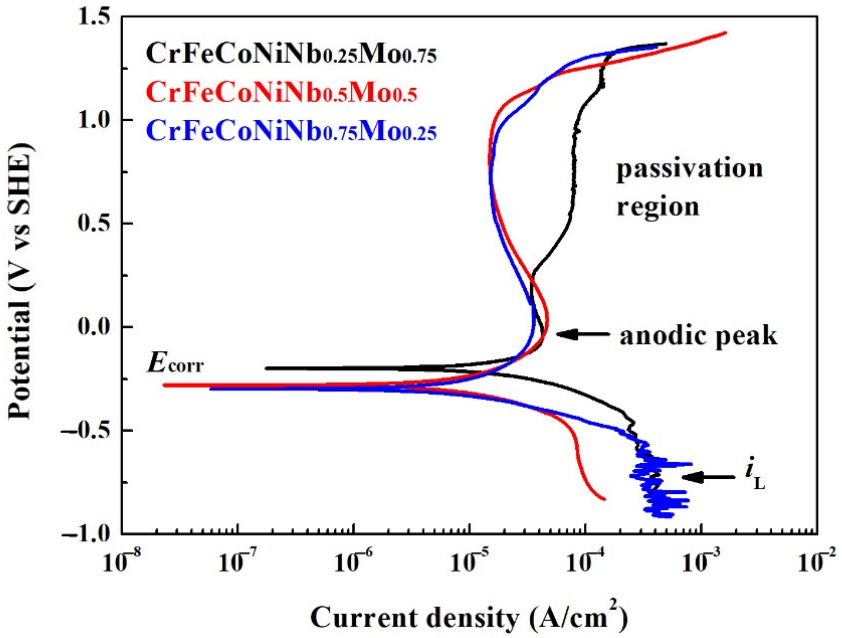

Figure 10. Potentiodynamic polarization curves of as-cast CrFeCoNiNb$_x$Mo$_{1-x}$ alloys tested in the 1 M deaerated sodium chloric solution at 30 °C.

Table 8. Potentiodynamic polarization data of the as-cast CrFeCoNiNb$_x$Mo$_{1-x}$ alloys in 1 M deaerated NaCl solution at 30 °C.

	CrFeCoNiNb$_{0.25}$Mo$_{0.75}$	CrFeCoNiNb$_{0.5}$Mo$_{0.5}$	CrFeCoNiNb$_{0.75}$Mo$_{0.25}$
E_{corr} (V vs. SHE)	−0.20	−0.28	−0.30
i_{corr} (μA/cm^2)	31.0	10.7	10.8
E_{pp} (V vs. SHE)	−0.04	0.03	0.03
i_{crit} (μA/cm^2)	43.2	47.0	36.0
i_{pass} (μA/cm^2)	34.4	15.0	15.6
E_b (V vs. SHE)	1.32	1.19	1.26

The corrosion rate of the alloys in deaerated 1 M H_2SO_4 and 1 M NaCl solutions can be calculated by assuming that all of the corrosion types of the alloys in these solutions are a type of uniform corrosion. Therefore, the relationship between corrosion depth of one year and corrosion current density is listed as the following Equation [27]:

$$\text{corrosiondepth} = \frac{M \cdot i_{corr} \cdot t}{\rho \cdot n \cdot F} \quad (1)$$

where M is the average atomic mass (g/mol), i_{corr} is the corrosion current density (A/cm^2), t is the corrosion time (31,536,000 s, 1 yr), ρ is the average density (g/cm^3), n is the number of average valence electron and F is the Faraday constant (96,500 C/mol). This study assumes that the average density of an alloy is $\rho = \sum X_i \rho_i$, where X_i and ρ_i are the molar fraction and density of element i. The corrosion rates (mm per year) of the alloys in deaerated 1 M H_2SO_4 and 1 M NaCl solutions are listed in Table 9. The CrFeCoNiNb$_{0.3}$Mo$_{0.3}$ alloy had the smallest corrosion rate (0.0732 mm/yr) in 1 M deaerated H_2SO_4 solution, and alloy CrFeCoNiNb$_{0.75}$Mo$_{0.25}$ had the largest corrosion rate (0.3315 mm/yr) in this solution. The CrFeCoNiNb$_{0.15}$Mo$_{0.15}$ alloy had the smallest corrosion rate (0.0425 mm/yr) in 1 M

deaerated NaCl solution, and $CrFeCoNiNb_{0.5}Mo_{0.5}$ and $CrFeCoNiNb_{0.75}Mo_{0.25}$ alloys had larger corrosion rate in this solution. The corrosion rate of $CrFeCoNiNb_{0.5}Mo_{0.5}$ alloy (0.1152 mm/yr) in 1 M deaerated NaCl solution was higher than that of $CrFeCoNiNb_{0.15}Mo_{0.15}$ alloy in the same solution. However, the $CrFeCoNiNb_{0.5}Mo_{0.5}$ alloy still possessed the best combination of corrosion resistance and hardness among these alloys.

Table 9. Corrosion rates of the as-cast alloys in deaerated 1 M H_2SO_4 and 1 M NaCl solutions at 30 °C.

Alloys	1 M H_2SO_4 (mm/yr)	1 M NaCl (mm/yr)
$CrFeCoNiNb_{0.15}Mo_{0.15}$	0.1204	0.0425
$CrFeCoNiNb_{0.3}Mo_{0.3}$	0.0732	0.1043
$CrFeCoNiNb_{0.25}Mo_{0.75}$	0.1091	0.0532
$CrFeCoNiNb_{0.5}Mo_{0.5}$	0.1077	0.1152
$CrFeCoNiNb_{0.75}Mo_{0.25}$	0.3315	0.1172

4. Conclusions

The microstructures, hardness and corrosion properties of hypoeutectic $CrFeCoNiNb_xMo_x$ alloys (x = 0.15 and 0.3) and hypereutectic $CrFeCoNiNb_xMo_{1-x}$ alloys (x = 0.25, 0.5 and 0.75) were studied. There were two phases (FCC and HCP) in these alloys. The dendrites of hypoeutectic $CrFeCoNiNb_xMo_x$ alloys (x = 0.15 and 0.3) were an FCC phase; the interdendrities of these alloys were a eutectic structure which the phases were HCP and FCC phases. The dendrites of hypereutectic $CrFeCoNiNb_xMo_{1-x}$ alloys (x = 0.25, 0.5 and 0.75) were an HCP-structured laves phase, and the interdendrities of these alloys were a eutectic structure with HCP and FCC phases. Increasing the content of Nb and Mo would increase the hardness of the alloys because of the formation of the hard HCP phase and the effect of solid solution strengthening. The $CrFeCoNiNb_{0.75}Mo_{0.25}$ alloy had the highest hardness of 625 HV among the alloys in present study. After potentiodynamic polarization test in deaerated 1 M H_2SO_4 and 1 M NaCl solutions at 30 °C, the $CrFeCoNiNb_{0.5}Mo_{0.5}$ alloy had the best corrosion resistance among these alloys by comparing the properties of corrosion potential, corrosion current density, anodic peak and passivation region of the alloys. Therefore, $CrFeCoNiNb_{0.5}Mo_{0.5}$ alloy was the best alloy among these alloys by comparing the corrosion properties and hardness.

Author Contributions: Conceptualization, C.-H.T.; methodology, C.-H.T., Y.-H.C. and M.-C.T.; formal analysis, C.-H.T., Y.-H.C. and M.-C.T.; investigation, C.-H.T., Y.-H.C. and M.-C.T.; data curation, C.-H.T., Y.-H.C. and M.-C.T.; writing—original draft preparation, C.-H.T.; writing—review and editing, C.-H.T.; supervision, C.-H.T. All authors have read and agreed to the published version of the manuscript.

Funding: This research received no external funding.

Institutional Review Board Statement: Not applicable.

Informed Consent Statement: Not applicable.

Data Availability Statement: Not applicable.

Acknowledgments: The authors are grateful to the Ministry of Science and Technology of the Republic of China for its financial support under the project MOST 110-2221-E-034-007.

Conflicts of Interest: The funders had no role in the design of the study; in the collection, analyses, or interpretation of data; in the writing of the manuscript, or in the decision to publish the results.

References

1. Murty, B.S.; Yeh, J.W.; Ranganathan, S.; Bhattacharjee, P.P. *High-Entropy Alloys*, 2nd ed.; Elsevier Co.: Amsterdam, The Nederlands, 2019; pp. 13–30.
2. Yeh, J.W. Alloy Design Strategies and Future Trends in High-Entropy Alloys. *JOM* **2013**, *65*, 1759–1771. [CrossRef]

3. George, E.P.; Raabe, D.; Ritchie, R.O. High-entropy alloys. *Nat. Rev. Mater.* **2019**, *4*, 515–534. [CrossRef]
4. Otto, F.; Dlouhy, A.; Somsen, C.; Bei, H.; Eggeler, G.; George, E.P. The influences of temperature and microstructure on the tensile properties of a CoCrFeMnNi high-entropy alloy. *Acta Mater.* **2013**, *61*, 5743–5755. [CrossRef]
5. Lu, K.; Chauhan, A.; Tirunilai, A.S.; Freudenberger, J.; Kauffmann, A.; Heilmaier, M.; Aktaa, J. Deformation mechanisms of CoCrFeMnNi high-entropy alloy under low-cycle-fatigue loading. *Acta Mater.* **2021**, *215*, 117089. [CrossRef]
6. Zhang, K.B.; Fu, Z.Y.; Zhang, J.Y.; Wang, W.M.; Wang, H.; Wang, Y.C.; Zhang, Q.J.; Shib, J. Microstructure and mechanical properties of $CoCrFeNiTiAl_x$ high-entropy alloys. *Mater. Sci. Eng. A* **2009**, *508*, 214–219. [CrossRef]
7. Senkov, O.N.; Wilks, G.B.; Scott, J.M.; Miracle, D.B. Mechanical properties of $Nb_{25}Mo_{25}Ta_{25}W_{25}$ and $V_{20}Nb_{20}Mo_{20}Ta_{20}W_{20}$ refractory high entropy alloys. *Intermetallics* **2011**, *19*, 698–706. [CrossRef]
8. Shkodich, N.; Sedegov, A.; Kuskov, K.; Busurin, S.; Scheck, Y.; Vadchenko, S.; Moskovskikh, D. Refractory High-Entropy HfTaTiNbZr-Based Alloys by Combined Use of Ball Milling and Spark Plasma Sintering: Effect of Milling Intensity. *Metals* **2020**, *10*, 1268. [CrossRef]
9. Vaidya, M.; Gariapati, M.M.; Murty, B.S. High-entropy alloys by mechanical alloying: A review. *J. Mater. Res.* **2019**, *34*, 664–686. [CrossRef]
10. Zhang, Y.; Li, R. New Advances in High-Entropy Alloys. *Entropy* **2020**, *22*, 1158. [CrossRef]
11. Xu, D.; Wang, M.; Li, T.; Wei, X.; Lu, Y. A critical review of the mechanical properties of CoCrNi-based medium-entropy alloys. *Microstructures* **2022**, *2*, 2022001. [CrossRef]
12. Muangtong, P.; Rodchanarowan, A.; Chaysuwan, D.; Chanlek, N.; Goodall, R. The corrosion behaviour of CoCrFeNi-x (x = Cu, Al, Sn) high entropy alloy systems in chloride solution. *Corros. Sci.* **2020**, *172*, 108740. [CrossRef]
13. Ma, G.; Zhao, Y.; Cui, H.; Song, X.; Wang, M.; Lee, K.; Gao, X.; Song, Q.; Wang, C. Addition Al and/or Ti Induced Modifications of Microstructures, Mechanical Properties, and Corrosion Properties in CoCrFeNi High-Entropy Alloy Coatings. *Acta Metall. Sin.* **2021**, *34*, 1087–1102. [CrossRef]
14. Godlewska, E.M.; Mitoraj-Królikowska, M.; Czerski, J.; Jawańska, M.; Gein, S.; Hecht, U. Corrosion of Al(Co)CrFeNi High-Entropy Alloys. *Front. Mater.* **2020**, *7*, 566336. [CrossRef]
15. Wang, W.; Wang, J.; Yi, H.; Qi, W.; Peng, Q. Effect of Molybdenum Additives on Corrosion Behavior of $(CoCrFeNi)_{100-x}Mo_x$High-Entropy Alloys. *Entropy* **2018**, *20*, 908. [CrossRef]
16. Hsu, W.C.; Kao, W.P.; Yeh, J.W.; Tsai, C.W. Effect of Mo on the Mechanical and Corrosion Behaviors in Non-Equal Molar AlCrFeMnNi BCC High-Entropy Alloys. *Materials* **2022**, *15*, 751. [CrossRef] [PubMed]
17. Tsau, C.H.; Chen, P.M. Corrosion Behavior of $Cr_{19}Fe_{22}Co_{21}Ni_{25}Mo_{13}$ Alloy in 1 M Nitric Acid and 1 M Hydrochloric Acid Solutions. *Crystal* **2021**, *11*, 1289. [CrossRef]
18. Mariano, N.A.; Souza, C.A.C.; May, J.E.; Kuri, S.E. Influence of Nb content on the corrosion resistance and saturation magnetic density of FeCuNbSiB alloys. *Mater. Sci. Eng. A* **2003**, *354*, 1–5. [CrossRef]
19. Tsau, C.H.; Yeh, C.Y.; Tsai, M.C. The Effect of Nb-Content on the Microstructures and Corrosion Properties of $CrFeCoNiNb_x$ High-Entropy Alloys. *Materials* **2019**, *12*, 3716. [CrossRef]
20. Tsau, C.H.; Lin, S.X.; Fang, C.H. Microstructures and corrosion behaviors of FeCoNi and CrFeCoNi equimolar alloys. *Mater. Chem. Phys.* **2017**, *186*, 534–540. [CrossRef]
21. Tsau, C.H.; Tsai, M.C.; Wang, W.L. Microstructures of FeCoNiMo and CrFeCoNiMo Alloys, and the Corrosion Properties in 1 M Nitric Acid and 1 M Sodium Chloride Solutions. *Materials* **2022**, *15*, 888. [CrossRef]
22. Bard, A.J.; Faulkner, L.R. *Electrochemical Methods: Fundamentals and Applications*, 2nd ed.; The Table on Inside Back Cover; John Wiley & Sons: New York, NY, USA, 2000.
23. Tsau, C.H.; Tsai, M.C. The Effects of Mo and Nb on the Microstructures and Properties of CrFeCoNi(Nb,Mo) Alloys. *Entropy* **2018**, *20*, 648. [CrossRef] [PubMed]
24. Smith, W.F. *Foundations of Materials Science and Engineering*, 3rd ed.; McGraw–Hill Co.: Singapore, 2004; pp. 877–878.
25. Chawla, S.L. *Materials Selection for Corrosion Control*; ASM International: Materials Park, OH, USA, 1993; p. 18.
26. Revie, R.W.; Uhlig, H.H. *Corrosion and Corrosion Control, an Introduction to Corrosion Science and Engineering*, 4th ed.; John Wiley & Sons: New York, NY, USA, 2008; p. 476.
27. Andrade, C.; Alonso, C. Corrosion rate monitoring in the laboratory and on-site. *Constr. Build. Mater.* **1996**, *10*, 315–328. [CrossRef]